Flow Instabilities in Gas Turbine Chute Seals

Joshua TM Horwood[1], Fabian P Hualca[1], Mike Wilson[1], James A Scobie[1], Carl M Sangan[1], Gary D Lock[1], Johan Dahlqvist[2] and Jens Fridh[2]

j.t.m.horwood@bath.ac.uk, f.hualca@bath.ac.uk, m.wilson@bath.ac.uk, j.a.scobie@bath.ac.uk, c.m.sangan@bath.ac.uk, g.d.lock@bath.ac.uk, jdahlq@kth.se and jens.fridh@energy.kth.se

[1]Department of Mechanical Engineering
University of Bath
Bath, BA2 7AY
United Kingdom

[2]Department of Energy Technology
KTH Royal Institute of Technology
Stockholm, Sweden

ABSTRACT

The ingress of hot annulus gas into stator-rotor cavities is an important topic to engine designers. Rim-seals reduce the pressurised purge required to protect highly-stressed components. This paper describes an experimental and computational study of flow through a turbine chute seal. The computations – which include a 360º domain - were undertaken using DLR TRACE's time-marching solver. The experiments used a low Reynolds number turbine rig operating with an engine-representative flow structure. The simulations provide an excellent prediction of cavity pressure and swirl, and good overall agreement of sealing effectiveness when compared to experiment.

Computation of flow within the chute seal showed strong shear gradients which influence the pressure distribution and secondary-flow field near the blade leading edge. High levels of shear across the rim-seal promote the formation of large-scale structures at the wheel-space periphery; the number and speed of which were measured experimentally and captured, qualitatively and quantitatively, by computations.

A comparison of computational domains ranging from 30º to 360º indicate that steady features of the flow are largely unaffected by sector size. However, differences

in large-scale flow structures were pronounced with a 60º sector and suggest that modelling an even number of blades in small sector simulations should be avoided.

1 INTRODUCTION

Successive generations of industrial gas turbines operate at increased thermal efficiency linked to increased turbine entry temperatures. The integral technology requires the evolving design of sophisticated secondary air systems that protect the integrity and operating life of critical components. Relatively cool sealing flow is diverted from the compressor to purge the *wheel-space* between stator and rotor discs. The purge flow pressurises the rotating cavities and reduces the undesirable *ingress* of hot gas from the mainstream annulus. Fitting rim seals at the periphery of these wheel-spaces limits the required sealing flow to control ingress; work is done on the extracted purge and superfluous use is inefficient. Designing ever-more effective rim-seals requires an understanding of the complex, three-dimensional flow driving ingress and egress through the seal clearances.

Recent experimental and computational research (*e.g.* [1-3]) has identified rim-seal instabilities featuring a range of frequencies below that of the blade passing frequency (BPF). These unsteady phenomena are driven by the vane-blade interaction and viscous shear, creating large-scale structures within or near the seal clearance. Data from the literature is shown in Figure 1, where the number of rotating structures (N) is plotted against their rotational speed relative to the disc (ω/Ω). This data is taken from experimental facilities operating over a wide range of Reynolds and Mach numbers; some facilities have vanes and blades, while others do not. The computational data stem from simulations using different sector sizes (including 360º) and turbulence models.

The new computational and experimental results from this paper have been added to the figure.

An understanding of how these structures influence rim-seal performance is important, and their unknown periodicity suggests that a reduced computational sector domain (*e.g.* 30º, 60º, 90º) might influence (or artificially enforce) *N*, and that a 360º domain should be used. The computational cost and time-frame for full 360º simulations may be prohibitive and beyond the feasibility of many industrial or academic applications.

This work provides guidance on the suitability of reduced computational domains for modelling ingress, informed by a closely-coupled experimental / computational investigation into steady and unsteady flow features in a *chute* seal, typical of many engines. The study presents original experimental and computation results from the University of Bath 1.5-stage test rig [4] with vane, blade and seal geometries modelled and scaled from the experimental facility at KTH Royal Institute of Technology [5]. More broadly, this work reports on the first phase of a collaboration with KTH to investigate the influence of scaling (Mach and Reynolds numbers) on ingress in gas turbines.

A literature review is presented in Section 2. The experimental test rig, computational model and operating conditions are described in Section 3. Sections 4 and 5 discuss both time-averaged and time-accurate results respectively. Section 6 gives the principal conclusions of the work.

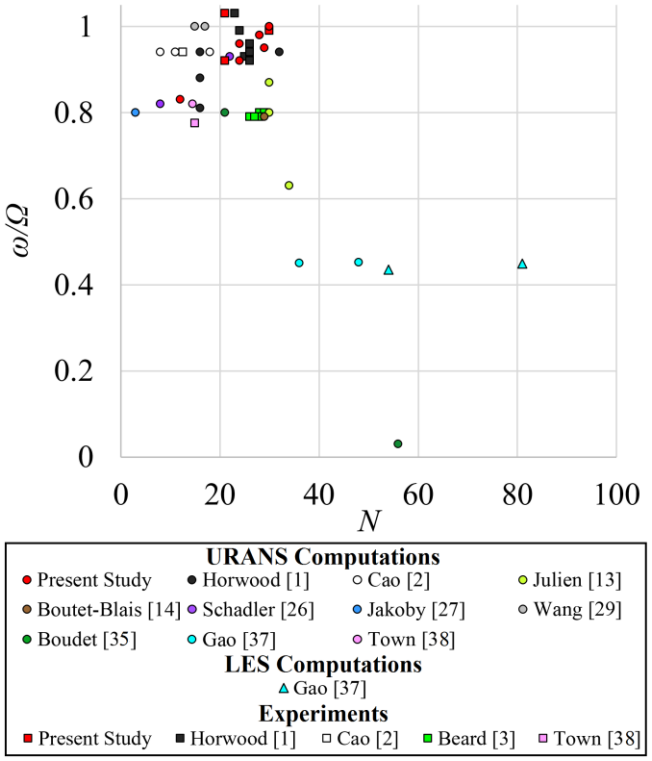

Figure 1: Rotating low-pressure structures from literature

2 LITERATURE REVIEW

Ingress in gas turbines has been studied experimentally and computationally for several decades. Interest from engine designers continues to reach unprecedented levels with major research facilities funded by engine companies around the globe. Scobie *et al.* [6] and Horwood *et al.* [1] provided recent reviews of experimental, analytical and computational studies. The review presented here is focussed principally on research published in the past five years, including that related to engine-realistic *chute* seals and the dependence of sector-size in computational studies.

2.1 Recent experimental and computational research

Scobie *et al.* [6], Savov *et al.* [7] and Mirzamogadam *et al.* [8] review fundamental investigations into the mechanisms of ingress using simple axial or radial rim-seal

clearances. Such idealised geometries are unlikely to be incorporated into engine designs. Scobie *et al.* [9] presented a seal design which evolved from a combined experimental and computational study at rig and engine conditions.

A chute seal is a common feature on stator and rotor platforms in operating engines, and this was the basis of computational work by Boudet *et al*. [10] and O'Mahoney *et al.* [11,12]. The latter focussed on the sensitivity of low-frequency unsteadiness in the rim-seal to sector size and mesh resolution, as discussed further in section 2.2. Boudet *et al.* [10] noted several flow features related to the chute seal. The egress and ingress through the angled seal was modulated by a region of high pressure from the passing blade. The swirl angle of the egress impinging upon the blade row was influenced by the sealing flow rate, with greater purge rates leading to higher fluctuations in swirl at the blade leading edge; this influence was even found downstream of the blades where distorted radial profiles of stagnation temperature were observed.

Julien *et al*. [13] and Boutet-Blais *et al*. [14] based their computations on the earlier experiments of Feiereisen *et al*. [15], which used a full-scale, half-span representation of the first stage in a modern high-pressure-ratio turbine. The experiments identified two unsteady structures per-revolution that was attributed to eccentricity in the disc. Both computational studies identified 24 - 34 large-scale flow structures rotating at less than the disc speed. Julien *et al*. [13] discussed how blade-vane interactions led to shallow ingress through the chute seal; however, only the large-scale structures (which were present at low and medium purge rates) led to ingress through a second radial clearance.

Gao *et al*. [16] simulated the experiments of Beard *et al*. [3], who used a rig that contained neither vanes nor blades. Gao *et al*. assessed the time-averaged flow within the overlapping gap of a chute seal. Reynolds-Averaged Navier-Stokes (RANS)

computations showed conventional rotor-stator behaviour: where the flow in the rotor boundary layer migrates outwards, and the flow in the stator boundary layer migrates inwards. However, Unsteady Reynolds-Averaged Navier-Stokes (URANS) and Large Eddy Simulations (LES) revealed a vortex structure rotating in the opposite direction to convention, with differences most pronounced for the LES. This vortex structure within the seal has been referred to as a Gap Recirculation Zone (GRZ) by Ko *et al*. [17] and Savov and Atkins [18], with the latter showing it is supressed and eventually 'blown out' as the purge flow rate is increased. Savov and Atkins also noted that, although not explicitly discussed, the GRZ could be observed in other studies, including that of Chilla *et al*. [19].

The computations of Chilla *et al*. [19] simulated the high-speed Rolls-Royce gas-turbine rig with engine representative sealing paths and blade geometry. The flow interaction at the rim-seal interface was shown to be influenced by the velocity deficit of the rim-sealing flow relative to that in the annulus, as well as by the circumferentially non-uniform pressure distribution imposed by the rotor blades. They emphasised the importance of rim-seal flow when analysing profiled end-walls due to the influence of purge on mainstream flow.

Near engine conditions were studied at facilities at Ohio State University (Green *et al*. [20, 21]) and Penn State University (Clark *et al*. [22], Berdanier *et al*. [23]). Green *et al.* [21] showed that purge flow creates aerodynamic blockage downstream of the high-pressure stator, increasing pressure on the vane suction surface and reducing tangential velocities exiting the vane row. Clark *et al.* [22] performed experiments with sealing flow injected through discrete inlet holes on the stator wall, identifying an influence of purge momentum. Berdanier *et al.* [23] extended the work of Clark *et al.*

[22] suggesting purge flow rates can be scaled given knowledge of the minimum purge flow rate required to fully seal the wheel-space.

Some facilities operate at Reynolds and Mach numbers well below that of an operating engine [4, 24]. Such experimental rigs offer a benign environment with improved access for instrumentation, flexible and expedient operation, reduced cost, and in some cases greater potential for insight to fundamental fluid dynamics and heat transfer. Teuber *et al*. [25] presented an extrapolation method to scale data from rigs operating at low Mach number to engine conditions with a geometrically similar turbine. The method is based on the assumption that the level of ingress is principally dependant on the peak to trough annulus pressure difference downstream of the vane.

2.2 Computational sector size

Horwood *et al.* [1] discussed the presence of structures in the rim-seal region; these instabilities may be larger than the blade pitch and rotate asynchronously to the rotor. The large-scale structures were identified by both experiment and computation, and their existence are thought to influence ingress. Many other authors (see Figure 1) have explored this phenomenon. Given the presence of these structures, the choice of computational sector size (*e.g.* 30º, 60º, 90º) is an important consideration when wishing to avoid an enforced periodicity potentially influencing the simulation. The majority of published computational work features a reduced sector, though a few have used the full 360º - *e.g.* [2, 8, 26, 27, 28, 29].

Cao *et al.* [2] were the first to identify these unsteady flow structures and investigate the influence of different sector sizes on their computations. They compared axisymmetric meshes of 360º and 90º. Despite the enforced periodicity of the sector model, the steady behaviour was largely unchanged and the unsteady structures were

very similar. Jakoby *et al*. [27] identified three large regions of low pressure in a 360º simulation which unsurprisingly were not captured in a small 22.5º sector due to the enforced periodicity. However, it should be noted that the larger structures identified by Jakoby *et al*. propagated deep into the cavity (indicating a potential cavity mode) which are distinct from those found by Cao *et al.* [2] (or Horwood *et al.* [1]) in the rim seal.

Zhou *et al.* [30] performed computations simulating the rig at Arizona State University. It was speculated that the underprediction of ingress was due to the use of a 14.4º sector that was unable to capture the rotating low-pressure zones predicted by 360º CFD; Wang *et al.* [29] computed (at low purge) the presence of 12 low-pressure zones in the rim-seal that were previously absent, precipitating increased ingress and lower stator-wall effectiveness in comparison to the sector model. Horwood *et al*. [1] demonstrated that it is possible to capture large-scale structures in a relatively small 22.5º sector, also finding an increased sector size of 67.5º made little impact upon both the unsteady flow structures and time-averaged results.

Several authors have performed LES of ingress; here sector size is of even greater importance due to the inherently larger computational requirements. O'Mahony *et al.* [11, 12] performed LES and URANS computations on various domains between 13.33º and 360º, concluding that 'URANS simulations on larger sector models, initialized from a single-sector model, showed little change in the frequency and amplitude of the unsteady pressure variations or ingestion.' These results suggest that sector size is not as important as turbulence modelling in the prediction of rim seal flows. Gao *et al.* [16] compared LES models of 13.3º and 24.8º, as well as URANS models of 24.8º and 360º (albeit without vanes or blades): they drew a similar conclusion to O'Mahony with

sector size showing little influence on both the time-averaged and unsteady flow characteristics.

Pogorelov *et al*. [28], to the authors' knowledge, is the only publication reporting a study of ingress using LES in a 360º model. A novel Cartesian meshing approach yielded results that compared well with time-averaged experimental data. However, no unsteady experimental data was provided for validation and the demanding computational requirement limited the simulations to a single flow condition.

3 CONFIGURATION AND NUMERICAL SETUP

The computations simulate the Bath University 1.5-stage turbine test rig and are supported by previously-unpublished experimental data. An overview of the experimental facility is given below. Full details of the rig design and capability have been presented by Patinios *et al.* [4].

3.1 Experimental Facility

The experimental facility was specifically designed to study ingress into the wheel-space cavities of an axial turbine. Incorporating a wide-range of instrumentation and designed in a modular fashion, the rig offers an expedient and inexpensive means of evaluating an advanced range of rim-seal concepts. The facility operates at fluid-dynamically scaled conditions at relatively low Reynolds numbers. Experiments match engine-representative values of the turbulent flow parameter (λ_T) and sealing flow parameter (Φ_0) which govern the wheel-space flow structure and levels of ingress respectively [31]. Typical operating conditions in non-dimensional form are presented in Table 1.

Parameter	Disk Speed (RPM)	
	3840	**5181**
Rotational Reynolds number, Re_ϕ	9.6×10^5	1.3×10^6
Axial Reynolds number, Re_w	3.4×10^5	4.6×10^5
Flow coefficient, C_F	0.35	
Vane exit Mach number, M	0.37	0.50
Turbulent flow parameter, λ_T	$0 \rightarrow 0.1$	
Non-dimensional sealing parameter, Φ_0	$0 \rightarrow 0.1$	

Table 1: Operating conditions

Flexibility of the seal, vane and blade geometries is an important feature of the facility. The profiles of the 48 stacked vanes and 60 turned blades, the chute seal, and the wheel-space geometry are based on a Siemens engine, geometrically scaled from the single-stage test facility at KTH Royal Institute of Technology [5]. This study did not include a second downstream row of vanes and only investigated the wheel-space upstream of the rotor. The outer radius of the wheel-space (b) is 190 mm, the annulus height is 25 mm and the minimum seal clearance in the chute seal (s_c) is 2.11 mm. The rig exhausts to atmospheric pressure.

A cutaway view of the rig test section, revealing the location of the key measurement instrumentation, is shown in Figure 2. Taps on the annulus hub allowed measurement of a circumferential distribution of static pressure downstream of the vanes. The radial distributions of static and total pressure in the wheel-space were acquired using taps on the stator wall and probes in the core; this enabled measurements of the radial distribution of swirl. The taps and probes also provided measurements of concentration-based sealing effectiveness by seeding the purge flow with 1% CO_2:

$$\varepsilon_c = \frac{c - c_a}{c_0 - c_a}$$

where c, c_a and c_0 are the local, annulus and purge concentrations of CO_2 respectively. The probes create a 1.6% blockage in the cross-sectional area of the instrumented outer wheel-space. Uncertainty analysis of the pressure and concentration measurements have been presented by Patinios *et al.* [4].

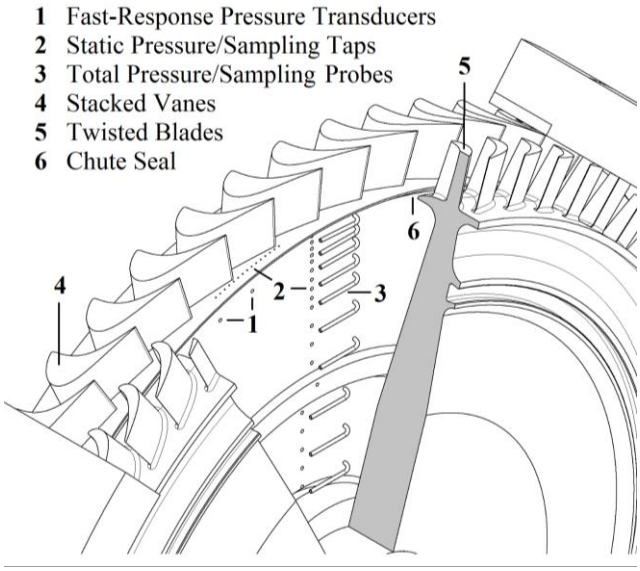

Figure 2: Experimental test section and instrumentation

A pair of Kulite XCS-062 pressure transducers were used to measure unsteady pressure fluctuations; these were fitted in the stator at a radial height of r/b = 0.958 - see Figure 2. By circumferentially offsetting these by 11.25° and performing phase analysis of the signals, the rotational speed of any large-scale instabilities could be calculated. The transducers were sampled at 100 kHz, and a 50 kHz low-pass filter was fitted upstream of the data-acquisition system to prevent aliasing. The transducer had a manufacturer-quoted resonant frequency of 150 kHz, which was significantly higher than the 5.2 kHz BPF at the highest rotational Reynolds number tested.

3.2 Computational Model

The computations presented here largely use the same modelling approach as the previous study of the same facility (albeit with different vane-blade-seal geometries) presented by Horwood *et al*. [1]. The Deutsches Zentrum für Luft- und Raumfahrt (DLR) turbomachinery specific code TRACE v9.0 was employed to run compressible Unsteady Reynolds-Averaged Navier-Stokes (URANS) computations using a finite-volume approach. Second-order temporal and spatial discretization was achieved with the Euler-backward and Fromm schemes. The shear stress transport (SST) turbulence model was implemented alongside the Kato-Launder production limiter. A passive scalar transport equation was used to model the CO_2 gas concentration in the experiments, providing a computational simulation of these measurements.

The dual time-stepping approach used 3840 time-steps per disc revolution, with 20 sub-iterations per time-step and a Courant-Friedrich-Levy number of 100; these values have previously been found to produce results insensitive to an increased number of timesteps [1].

NUMECA AutoGrid5 was used to generate the structured grid. Mesh detail is shown in Figure 3. In the radial direction, the vane and blade passages incorporate 49 and 60 nodes respectively, while in the circumferential direction they include 66 and 63 nodes at exit. The blade tip gap spans 15 nodes and there are 43 nodes across the seal clearance. Boundary layers were solved using a $y+ \sim 1$ on the annulus hub and wheel-space surfaces; wall functions were employed at the less critical vane, blade and shroud surfaces with $y+ \sim 25$. A grid-dependence study, detailed by Horwood *et al*. [1] showed no distinguishable differences between results from a baseline and refined grid; the mesh used in the current study follows all the same design principles as this baseline grid.

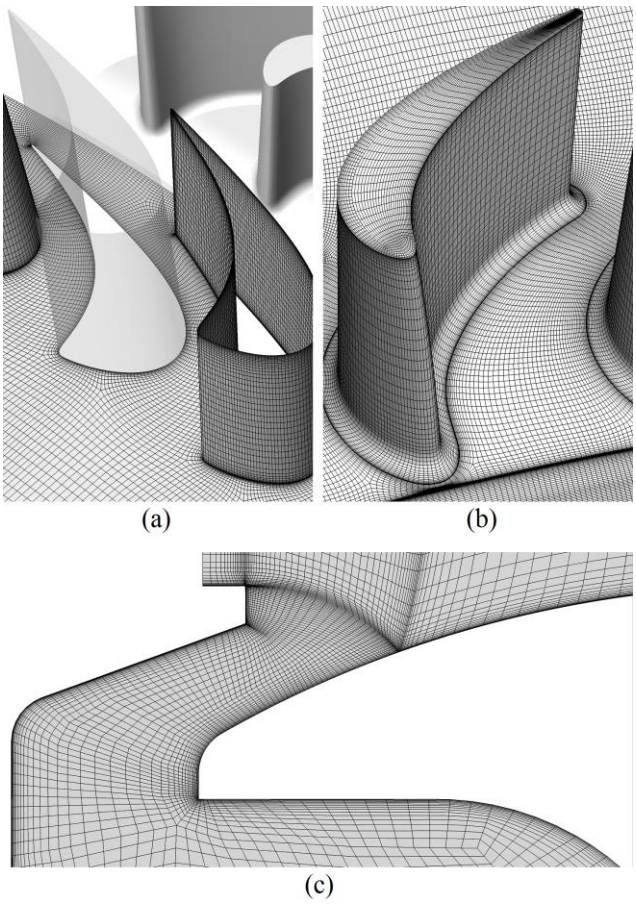

Figure 3: Mesh detail: (a) vane row, (b) blade row, (c) chute seal

Solutions were computed only at the higher experimental Reynolds number ($Re_\phi \sim 1.3 \times 10^6$) to restrict cost. The bulk of the results presented in this paper use a sector model incorporating four vanes in a stationary domain, and five blades along with the wheel-space in a rotating domain - see Figure 4. These domains are separated by a non-matching interface 1 mm upstream of the seal. This 30º sector contains 6.7×10^6 cells. However, baseline results are compared to computations using 60º, 90º and 360º sectors, each created by duplicating the smaller sector. The maximum mesh size was 80.7×10^6 cells. Total temperature, turbulence intensity, turbulence length scale and flow angles were specified at both inlets in addition to total pressure at the stage inlet and mass-flow at the sealant inlet. Static pressure was specified at the stage outlet.

Steady mixing-plane solutions were used to initialise each of the 30º unsteady calculations. Once converged these were duplicated and used to initialise the unsteady larger-sector models. Larger-sector models were subsequently computed for a minimum of seven revolutions to allow flow changes to develop fully. All solutions achieved < 1% change in ε_c over 20,000 timesteps alongside periodic, unchanging behaviour in other variables. Average residual levels were < 10^{-6} and maximum residual levels < 10^{-3}.

Computational costs were highest for the low purge flow cases, due to the slow convection of the passive scalar; the 30º sector required > 30 revolutions, equating to ≈ 60,000 core hours. For comparison, the additional 10 revolutions computed with the 360º model required ≈ 320,000 core hours.

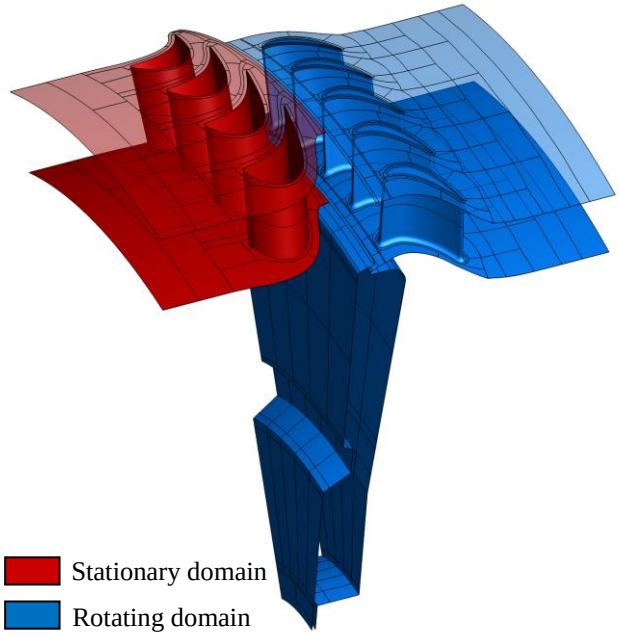

Figure 4: 30º computational domain

4 TIME-AVERAGED RESULTS

This section presents and discusses steady results, with unsteady phenomena shown in Section 5. Experimental and computational comparisons include interrogation of

pressure, velocity and sealing effectiveness. The section is sub-divided as follows: annulus (4.1), rim-seal (4.2) and wheel-space (4.3). Computational results are based on the 30º sector model, except where explicitly stated otherwise.

4.1 Annulus pressure distribution

Figure 5 illustrates the variation of time-averaged pressure coefficient ($C_{p,a}$) with normalised circumferential position across a vane passage in the annulus. The definition of $C_{p,a}$ and other variables are included in the nomenclature. The data were collected on the hub 1.2 mm downstream of the vanes, as depicted in the silhouette. The positions for data collection are also seen in Figure 2. The experimental data were collected across three vane passages, measured from two instrumented regions separated by 180°. The computed values of $C_{p,a}$ (shown across four vane pitches) were determined from the 30º sector model; however, no identifiable differences were found using four sector sizes (30º, 60º, 90º, 360º). The agreement between computational and experimental results is good and provides confidence that the CFD has accurately captured the pressure distribution in the annulus. All data is presented for a non-dimensional sealing flow rate, Φ_0 (see nomenclature for definition), of 0.075, although very similar agreement was found across all purge rates tested. Note there is a second-order effect of Φ_0 on distribution of $C_{p,a}$ often referred to as the *spoiling effect*, Da Soghe *et al*. [32].

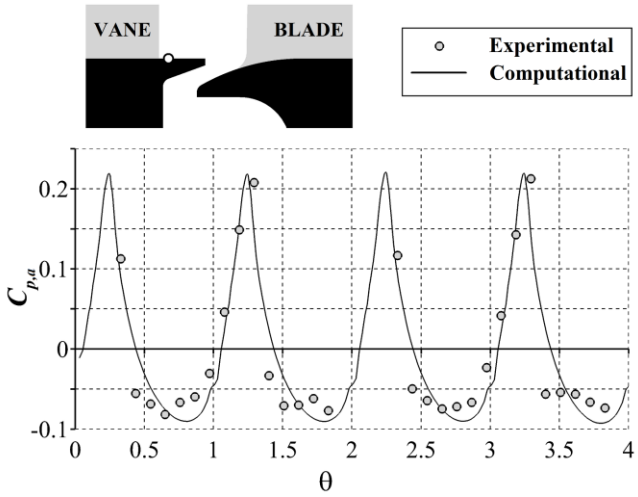

Figure 5: Circumferential distribution of time-averaged pressure coefficient over four vane pitches (Φ_0 = 0.075)

4.2 Time-averaged flow in the chute seal

Figure 6 illustrates time- and circumferentially-averaged profiles of computed velocity across the chute seal; the data is extracted along the dashed line. In each plot the ordinate is aligned with the angled, outer-overlap region of the stator wall and the abscissa represents the location across the seal gap with the silhouettes scaled appropriately. The ordinate represents the tangential velocity for (a) and (c), and the stream-wise velocity for (b) and (d); the velocity is normalised by the disc speed (Ωb) in all cases.

Comparisons of velocity profiles for four different domain sizes are shown in Figure 6 (a) and (b), with all sectors computed at Φ_0 = 0.05. It can be seen there is no significant effect of sector size on the tangential velocity profiles, with only a minor effect on the stream-wise velocity. However, it should be noted that the largest discrepancy relative to the 360º computation is seen in the 60º sector model while the smallest differences are with the 90º sector model; this is also reflected in sealing effectiveness discussed in

Section 4.3. These dissimilarities are believed to be a result of discrepancies between the unsteady flow phenomena captured in each simulation, as discussed in Section 5.

The normalised tangential velocities in Figure 6 (c) illustrate the mean swirl across the seal decreases with increasing purge flow rate. Steep velocity gradients are observed in the stator and rotor boundary layers outside the core flow, following standard theory for a stator-rotor system. However, in the stream-wise velocity components, seen in plot (d), the bulk flow exiting the seal does so along the stator and the bulk flow ingested through the seal is attached to the rotor. This flow configuration challenges the conventional arrangement expected for a Batchelor flow regime where flow is pumped radially outward in a rotor boundary layer and migrates inward in a stator boundary layer. The computed flow structure is consistent with a recirculating flow feature within the seal, referred to as a GRZ by numerous authors - see section 2.1. Similar profiles of velocity were shown by Gao *et al*. [16] who argued that the seal recirculation may be interpreted as evidence for the existence of Taylor-Couette vortices.

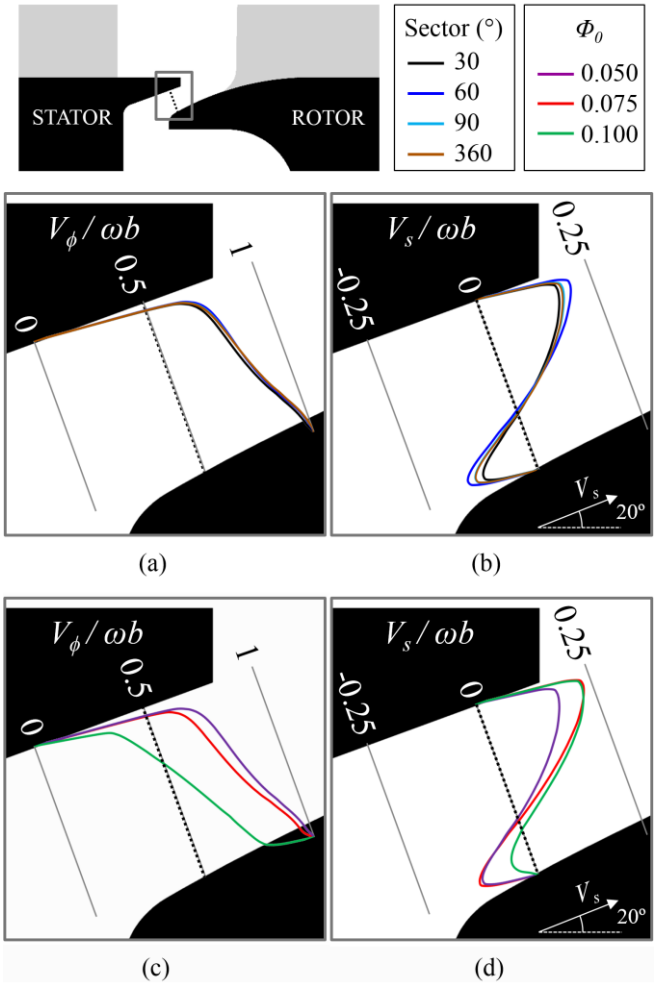

Figure 6: Computational profiles of tangential velocity (a/c) and stream-wise velocity (b/d) across the chute seal: (a/b) sector size comparison at Φ_0 = 0.05, (c/d) Φ_0 comparison with a 30° sector

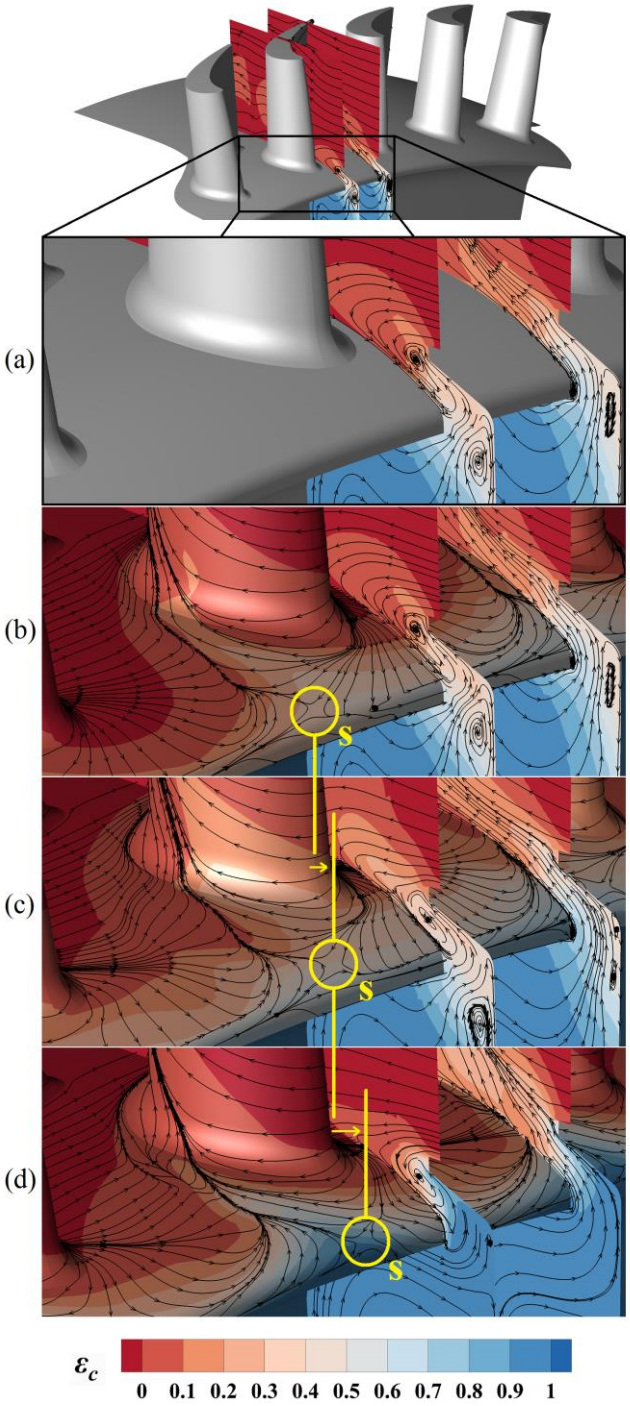

Figure 7: Time-averaged streamlines in the rotational frame from a 30º sector model, 'S' indicates saddle points: (a, b) Φ_0 = 0.050, (c) Φ_0 = 0.075, (d) Φ_0 = 0.100

Figure 7 (a) shows *streamlines* on two circumferential planes aligned with regions of peak ingress and egress. Figure 7 (b-d) show additional *streak-lines* on the rotor hub

and blade surfaces for three different purge flow rates. The contours represent sealing effectiveness with all data temporally averaged in the rotational frame over a single disc rotation. Figure 7 indicates that with increasing purge the vortex in the seal clearance is modulated circumferentially by the rotor blades and is not present in the centre of the passage where the egress flow is at its maximum (right-hand plane). The wall streak-lines indicate the gap recirculation interacts directly with the leading-edge horseshoe vortex on the blade; this suggests the proximity of the blade to the chute seal affects the seal recirculation and influences ingress. Further secondary flow features are illustrated in Figure 7, including the radial migration of the passage vortex up the suction surface of the blade (which could provide a tangible cooling effect to the blade) and the displacement of the saddle point. This saddle point (labelled S) has a clear dependence on sealing flow rate, moving further right (against the direction of rotation) with increasing purge. Surprisingly, the suction surface of the blade shows a higher sealing effectiveness at $\Phi_0 = 0.075$ (plot c), than at $\Phi_0 = 0.100$ (plot d): this is due to the egress separating from the rotor surface for conditions with higher purge momentum.

The influence of egress on both the annulus fluid dynamics and rotor surface temperature is clearly significant, indicating the importance of considering both seal geometry and purge rate when designing annulus features such as profiled end-walls.

Figure 7 illustrates tangential streamlines in two cross-sections of the chute seal but not the level of shear that exists in the azimuthal direction. At the exit of the chute seal, the highly-turned annulus flow downstream of the vanes shears the relatively low swirl in the cavity. Several authors have proposed different hypotheses for the fundamental driver of large-scale structures in the seal [1, 7, 33]. Two proposals are that they arise from Taylor-Couette or Kelvin-Helmholtz instabilities; both explanations are a result of shear. Figure 8 shows time-averaged computational velocity vectors from three

azimuthal locations through the seal, at three purge rates. The location of each set of vectors, time-averaged in the rotational frame, follows the dashed line in the silhouette. The vectors are shown to reverse in direction as the cavity fluid rotates slower than the disc and the annulus flow swirls faster than the disc. Figure 8 (b) shows there is a strong radial gradient in swirl extending from below the rotor platform, through the seal and into the annulus. The magnitude of the shear gradient, and radial and azimuthal position varies with purge flow. The gradient is strongest at higher purge rates and the position of maximum gradient is forced radially outwards; this is consistent with higher purge being associated with less momentum exchange between the annulus and wheel-space.

4.3 Time-averaged wheel-space flow

Figure 9 directly compares experimental and computational profiles of swirl through the wheel-space. The results are presented at four values of λ_T, the turbulent flow parameter which governs the boundary layers in the wheel-space [31]. The figure shows excellent agreement between experimental and computational results and provides validation that the cavity flow has been computed accurately. The figure also shows how the tangential velocity throughout the wheel-space is supressed with an increasing sealing flow rate, as expected.

Further confidence in the computation of pressure in the wheel-space flow can be gained from Figure 10, which depicts radial profiles of pressure coefficient on the stator wall in the cavity – $C_{p,s}$ is defined in the nomenclature. The data are presented at four sealing flow rates. As the wheel-space is pressurised with increasing purge, the radial variation in pressure is reduced.

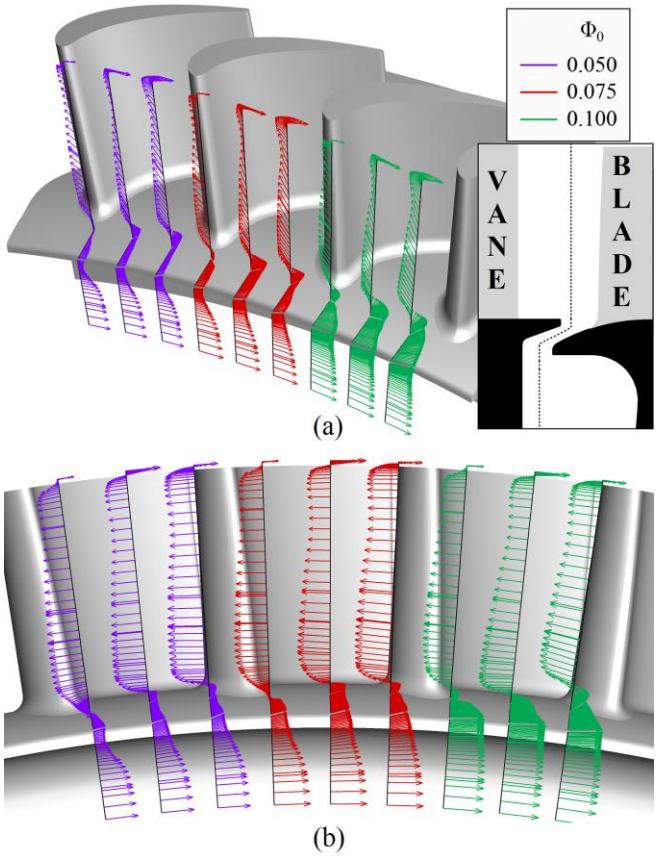

Figure 8: Velocity vectors through the seal (rotational frame) at three levels of purge

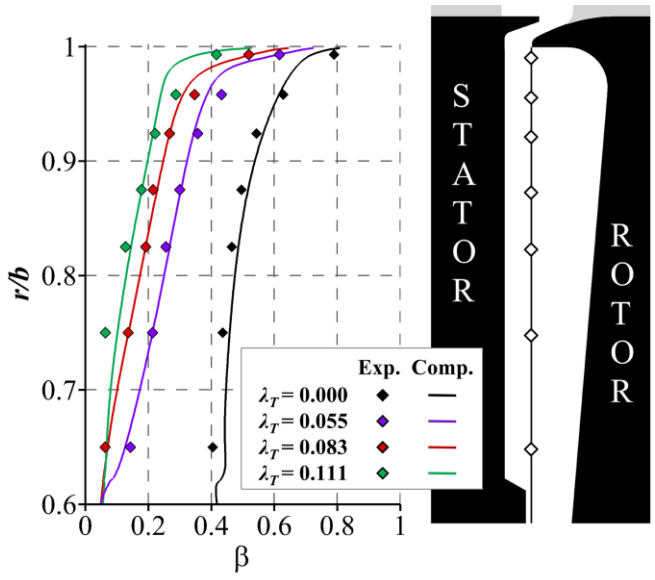

Figure 9: Radial distribution of swirl in the wheel-space at four levels of purge

Figure 11 (a/b/c) shows the radial variation of ε_c at Φ_0 = 0.050, 0.075 and 0.100 respectively (*i.e.* increasing purge). Results from the stator wall and rotating core are depicted discretely by circle and diamond symbols (respectively) for the experiments, alongside continuous solid and dashed lines (respectively) for computations. The right-hand silhouettes are aligned with the radial position of the ordinate and include superimposed contours of computed sealing effectiveness. Though not shown here, the experimental data is invariant with Reynolds number for the two conditions tested in Table 1.

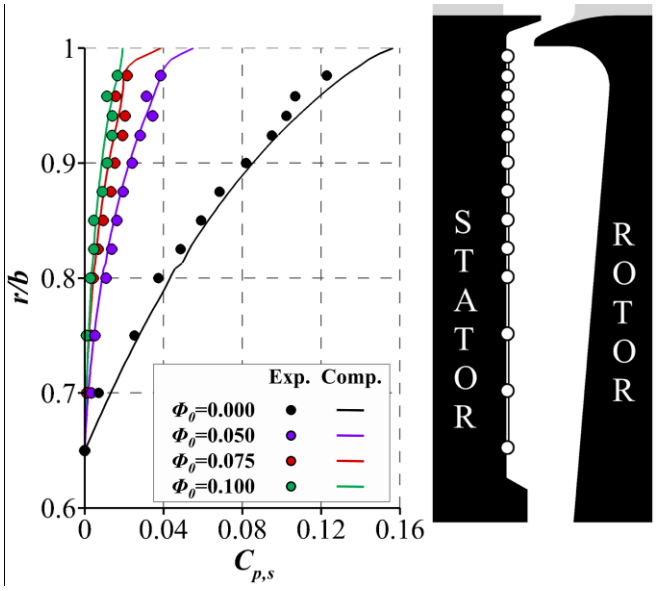

Figure 10: Radial distribution of stator-wall pressure coefficient at four levels of purge

At the two lower sealing flow rates (Figure 11 a/b) there is generally good agreement between the quantitative levels of ingress seen experimentally and computationally. The data and contours show abrupt increases in ε_c across the chute seal where the free-stream effectiveness in the annulus is zero. Relatively high gradients of sealing effectiveness exist in the wheel-space at high radius ($1 > r/b > 0.8$). This behaviour departs from the classic Batchelor-type flow structure where a stator wall boundary

layer drives a radially-invariant distribution of effectiveness. Instead, there is a large mixing region where ingested fluid is diluted by the sealing flow pumped up the rotor boundary layer, with differences in concentration between the core and the stator. This flow structure is thought to be more prominent than in previous studies of the same rig (*e.g.* [4]) because the chute seal encourages the rotor boundary layer to impinge directly upon the stator wall. At $r/b < 0.8$, the radial gradient of ε_c is significantly reduced, with core and stator wall at the same concentration.

Figure 11 (c) shows a qualitatively similar flow structure but weaker agreement between experiment and computation at high purge. This discrepancy is discussed in the context of Figure 12 below.

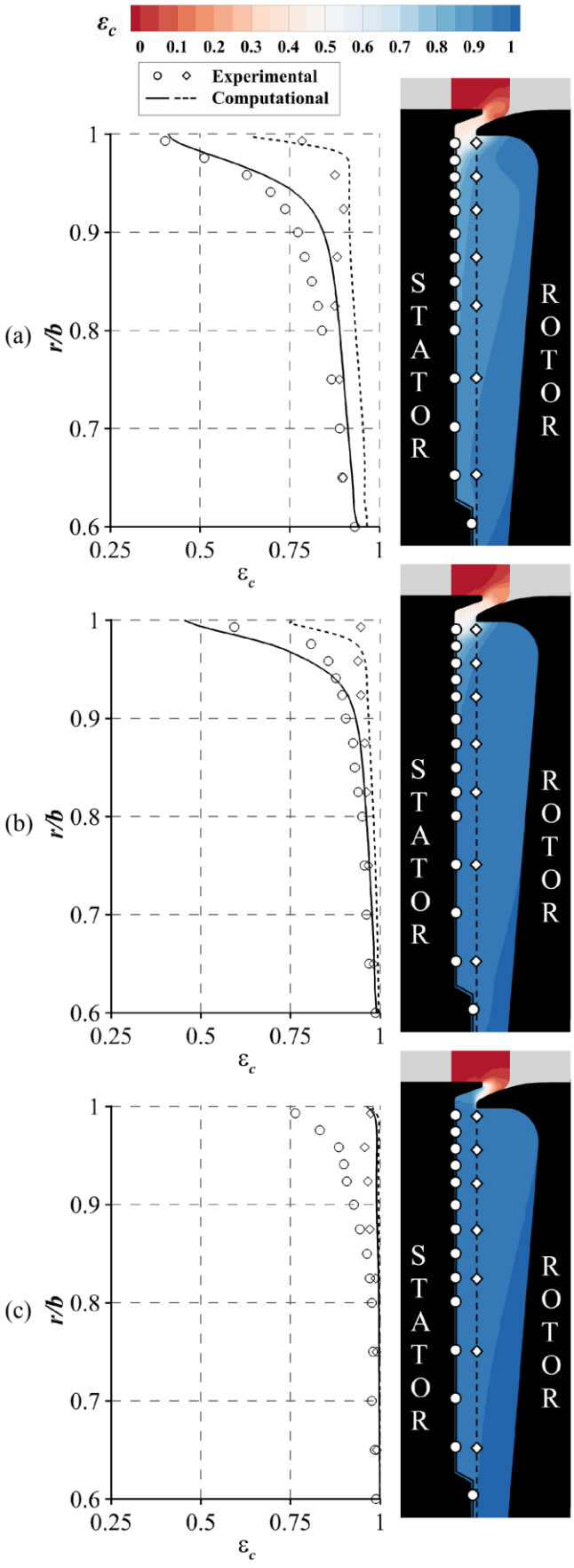
ε_c
0 0.1 0.2 0.3 0.4 0.5 0.6 0.7 0.8 0.9 1
Experimental
Computational
(a)
(b)
(c)
r/b
1
0.9
0.8
0.7
0.6
0.25
0.5
0.75
1
ε_c
STATOR
ROTOR

Figure 11: Radial distribution of concentration-based sealing effectiveness in the wheel-space: (a) Φ_0 = 0.050 (b) Φ_0 = 0.075 (c) Φ_0 = 0.100

Figure 12 shows the variation of ε_c on the stator wall with sealing flow parameter; the experimental and computational data is shown at r/b = 0.958 and 0.85. Generally, the sealing effectiveness increases with Φ_0 as the purge pressurises the wheel-space and reduces ingress. Experimental data are presented at two differing rotational speeds, largely collapsing with an insensitivity to Reynolds number. There is an inflexion in the experimental data for 0.06 < Φ_0 < 0.12, which is qualitatively similar to experimental data reported elsewhere [1, 22, 34, 35]. Here the data has been collected at a flow coefficient C_F = 0.35, which is the design point for the stage; the degree of inflexion is sensitive to flow coefficient, and has not been accurately captured computationally, leading to the mismatch in sealing effectiveness in Figure 11 (c). Horwood *et al.* [1] related the inflexion to strong unsteady pressure structures close to the rim seal. Further work, presented by Hualca *et al*. [36], has shown the unsteadiness and inflexion disappear when the blades are removed from the rig and it is speculated that the two features are closely related. The unsteady data are discussed further in Section 5.

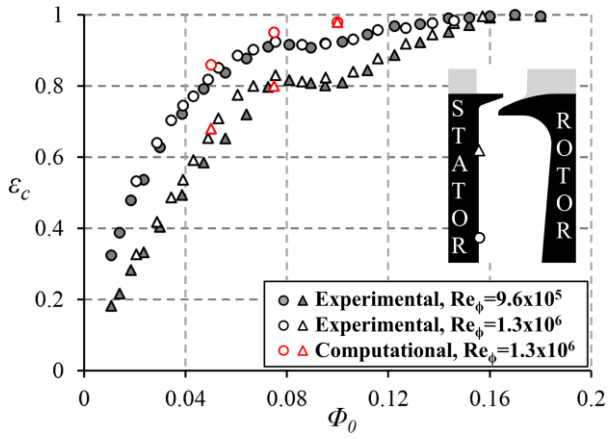

Figure 12: Variation of stator effectiveness with non-dimensional sealing parameter

Computational profiles of the radial variation of ε_c on the stator wall for four different sector sizes are presented in Figure 13. All results are shown for $\Phi_0 = 0.05$. For $r/b > 0.9$ small differences in ε_c are apparent in all sector models in comparison with the 360º case. The most pronounced differences are for the 60º sector. This feature is also reflected in the seal velocities shown in Figure 6 (b), and again can be attributed to the discrepancies between the unsteady flow phenomena captured in each simulation (see section 5.2). However, at lower radius the curves collapse well and despite the differences in unsteady structures the degree of ingress is broadly invariant to sector size. Note that the corresponding experimental data are displayed in Figure 11 (b).

5 UNSTEADY FLOW PHENOMENA

Cao *et al.* [2] first identified rim-seal flow structures spanning more than a single vane or blade pitch, and numerous authors have subsequently reported similar effects. However, no research has conclusively identified the physical cause of such phenomena. This section presents unsteady computational and experimental data over a range of conditions and discusses the influence of sealing flow rate and computational sector size on the results.

5.1 Sensitivity to sealing flow rate

Figure 14 and Figure 15 show Fast Fourier Transformations (FFTs) of computational and experimental results respectively. The FFTs are based on unsteady pressure from the stator wall at $r/b = 0.958$, as shown in the silhouettes. Four purge flows are used ($\Phi_0 = 0$, 0.05, 0.075 and 0.10) at $\mathrm{Re}_\phi = 1.3\times10^6$. All computations in Figure 14 are based on a 30º sector. Frequencies have been normalised against f_d (the rotating disc frequency) and the pressure has been normalised as C_p (a pressure coefficient defined in the

nomenclature). All results were extracted in the stationary frame: computationally this required processing data from the rotating domain over the final disc revolution using the method described by Horwood *et al*. [1]. Experimental results were invariant across both Re_ϕ listed in Table 1, with data presented only at $Re_\phi = 1.3\times10^6$ for reasons of clarity.

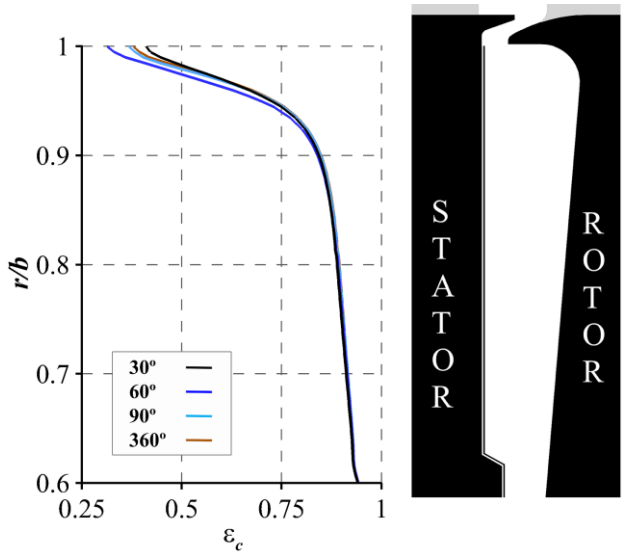

Figure 13: Radial distribution of concentration-based sealing effectiveness in the wheel-space at Φ_0 = 0.050: sector size comparison

Consider Figure 14. Increased activity is generally observed at $f / f_d = 60$ which corresponds to the BPF. Spectral activity at frequencies below the BPF exist at all computed sealing flow rates with the peak frequency and amplitude varying with purge. At $\Phi_0 = 0$, the peak frequency of 40 corresponds to $N = 36$ structures rotating at $\omega/\Omega \sim 1.11$. It should be noted that $\omega/\Omega > 1$ is possible given $\beta > 1.5$ immediately downstream of the vanes. This frequency reduces to 23 ($N = 24$ rotating at $\omega/\Omega \sim 0.96$) at $\Phi_0 = 0.05$; at higher purge these unsteady pressure signals are more intense. The magnitude of the peak signal increases further at $\Phi_0 = 0.075$, while the speed of the corresponding structures reduces to $\omega/\Omega \sim 0.92$. At the highest purge ($\Phi_0 = 0.100$) there is a significant

reduction in strength and frequency: $f/f_d = 10$, corresponding to $N = 12$ and $\omega/\Omega \sim 0.83$. Further peaks in each of the plots are due to harmonics and nonlinear combinations of the peak low frequency and the BPF: (a) 20 = 60 - 40, (b/c) 37 = 60 - 23, (d) 20 = 10 × 2. Note that information regarding N and ω/Ω is tabulated in Table 2 and shown in Figure 1. These structures are visualised in Figure 17 and discussed further in Section 5.2.

Figure 14 and Figure 15 allow a direct comparison between computational and experimental frequencies at common purge. The experiments also clearly measure activity at the BPF for all cases. Although experimentally-determined frequencies < BPF are largely supressed at $\Phi_0 = 0$ and 0.1, the computations have captured numerous qualitative and quantitative similarities. There are similar peak frequencies that reduce with increasing purge and are most intense at $\Phi_0 = 0.05$ and 0.075. It is speculated that with lower purge the intensity of the instabilities is reduced due to the relatively weak shear gradient between annulus and wheel-space. At high purge the egress through the seal dominates the fluid dynamics, simply blowing out any large-scale structures. The experimental FFTs offer significantly higher resolution. This is a result of experimentally sampling from ~ 860 revolutions; the computational sampling is limited to a single disc revolution.

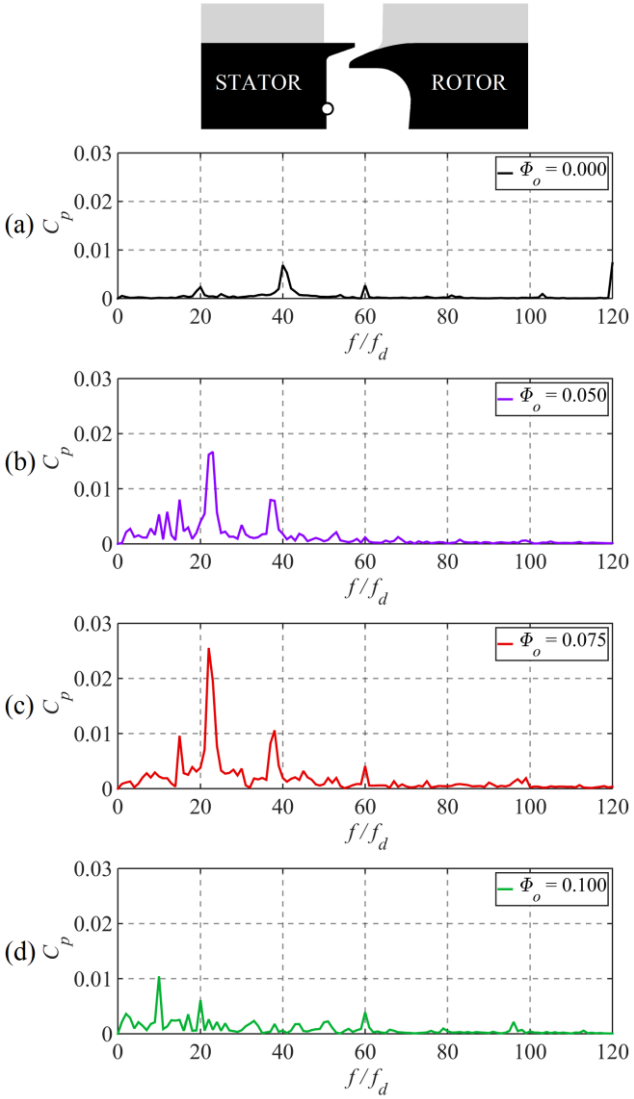

Figure 14: Fast Fourier Transforms of computational data using a 30º sector at $Re_\phi = 1.3\times10^6$

Phase analysis was performed over signals from two pressure transducers offset by 11.25° (α) in the azimuthal direction. This allowed measurement of the number of structures (N) and their rotational speed (ω/Ω). Data were sampled at 100 kHz over 10 s and divided into single disc revolutions. The two signals were cross-correlated for each revolution to determine a lag time, with the value for each revolution populated on a histogram. This allows calculation of the average lag time (Δt_α) and leads to the

rotational speed ($\omega = \alpha / \Delta t_\alpha$). The number of structures around the disk (N) is calculated from the normalised frequency (f/fd) divided by the normalised rotational speed (ω/Ω).

The data are shown in Table 2 alongside computed values. Computationally, at Φ_0 = 0.05 and 0.075, N = 24, which compares well the measured value, N = 21. Equally the computed speed reduces from $\omega/\Omega \sim 0.96$, to $\omega/\Omega \sim 0.92$, comparing well with the experimental speed reducing from $\omega/\Omega \sim 1.03$, to $\omega/\Omega \sim 0.92$. It should be noted that the absolute amplitudes of the computed low-frequency structures are significantly higher than those measured. This is believed to be a result of RANS turbulence modelling, where the greater viscosity term can give rise to more stable vortical structures. Despite this, the overall behaviour of the CFD is encouraging and provides clear insight into the unsteady fluid dynamics.

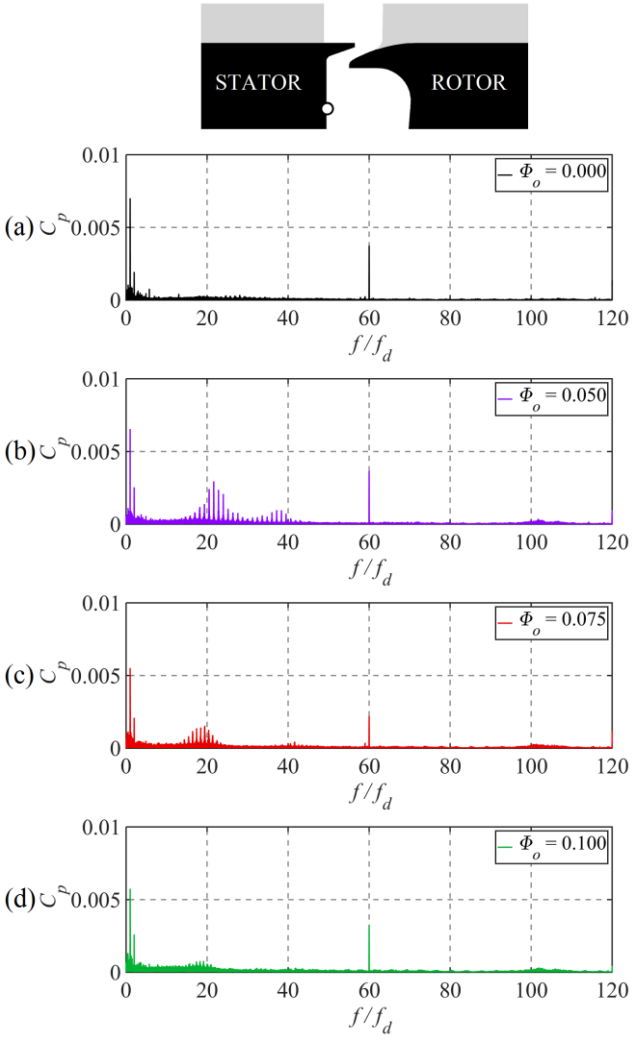

Figure 15: Fast Fourier Transforms of experimental data at $Re_\phi = 1.3\times10^6$

Several authors have proposed hypotheses for the physical origin of the large-scale structures measured and computed here. The two most compelling arguments for the driving mechanism are that they arise from Taylor-Couette or Kelvin-Helmholtz instabilities. Both explanations are fundamentally based on shear: the overlapping stator and rotor surfaces in the case of the Taylor-Couette instabilities (see Figure 6) or by differences in the levels of swirl in the wheel-space and annulus for the case of Kelvin-Helmholtz instabilities (see Figure 8). The results here do not prove either of these

hypotheses correct, but clearly flow through the rim-seal is subjected to significant three-dimensional shear.

Case	Non-dimensional Sealing Parameter (Φ_0)	Approximate number of structures (N)	Rotational speed of structures (ω/Ω)
Comp. (30º)	0.000	36	1.11
Comp. (30º)	0.050	24	0.96
Comp. (30º)	0.075	24	0.92
Comp. (30º)	0.100	12	0.83
Comp. (60º)	0.050	30	1
Comp. (90º)	0.050	28	0.98
Comp. (360º)	0.050	29	0.95
Exp.	0.000	N.A	N.A.
Exp.	0.050	21	1.03
Exp.	0.075	21	0.92
Exp.	0.100	N.A	N.A.

Table 2: Large scale flow structures

5.2 Sensitivity to sector size

Sector models facilitate the use of CFD at significantly-reduced cost with expedience. Section 5.1 presented unsteady computations using a 30º sector model not untypical of many industrial operations. However, the inherent periodicity in such simulations can

influence the calculation of fluid-dynamic structures larger than a vane or blade passage.

FFTs of unsteady pressure at locations close to the rim seal are presented for sectors of 30º, 60º, 90º and 360º in Figure 16. Data is shown for Φ_0 = 0.05 at three radial locations. The results are normalised using the same method described above for Figure 14. Spectral peaks at f / fd = 60, correspond to the BPF and increase in intensity as the monitoring point moves radially outwards through the seal clearance towards the blades. There is a range of frequencies below the BPF, indicating large-scale structures. There are differences in the characteristics of these instabilities when they are computed using different sector sizes. Across all domain sizes, the intensity of spectral activity is observed to be strongest within the chute seal, in the proximity of strongest shear.

The frequency spectra for the 90º and 360º domains show consistent behaviour at all three locations in the simulations. The dominant structures in each correspond to N = 28 rotating at $\omega/\Omega \sim 0.98$ and N = 29 rotating at $\omega/\Omega \sim 0.95$ respectively. For the 30º sector the computations output N = 24 rotating at $\omega/\Omega \sim 0.96$, and for the 60º sector N = 30 rotating at $\omega/\Omega \sim 1.00$. This data is shown in Table 2.

The number of structures in each sector model converge towards that from the 360º simulation, but retain an integer number of structures in each sector due to the enforced periodicity. For the 30º sector (1/12th of the full 360º) N must be a multiple of 12, and 24 is the closest value to 29. For the 60º sector (1/6th of the full 360º) N must be a multiple of 6, and 30 is the closest value to 29. For the 90º sector (1/4th of the full 360º) N must be a multiple of 4, and 28 is the closest value to the 29.

The 60º simulation exhibits behaviour which departs from that produced by other sector sizes. There is a significant peak amplitude at exactly half the BPF, with structures rotating at precisely the disc speed. This is enforced artificially by the

periodicity and leads to the largest discrepancies when the time-averaged results for the sector models are compared to the 360º simulations in Figure 6 and Figure 13. To prevent this enforced periodicity, small-sector models should avoid using an even number of blades to preclude the possibility of one structure existing per two blade passages.

The computed large-scale structures are visualised in Figure 17, using contours of instantaneous sealing effectiveness on a plane through the chute seal. Figure 17 (a)-(d) show enlarged views of the 30º, 60º, 90º and 360º models respectively. The increased regularity of the structures that align with every second blade for the 60º sector model is clearly visible in (b), contrasting with the more similar structures for the other sectors. Figure 17 (e) presents the 360º simulation with an additional iso-surface of ε_c = 0.025, indicating the coupling between egress and the contoured planes shown in plots (a)-(d).

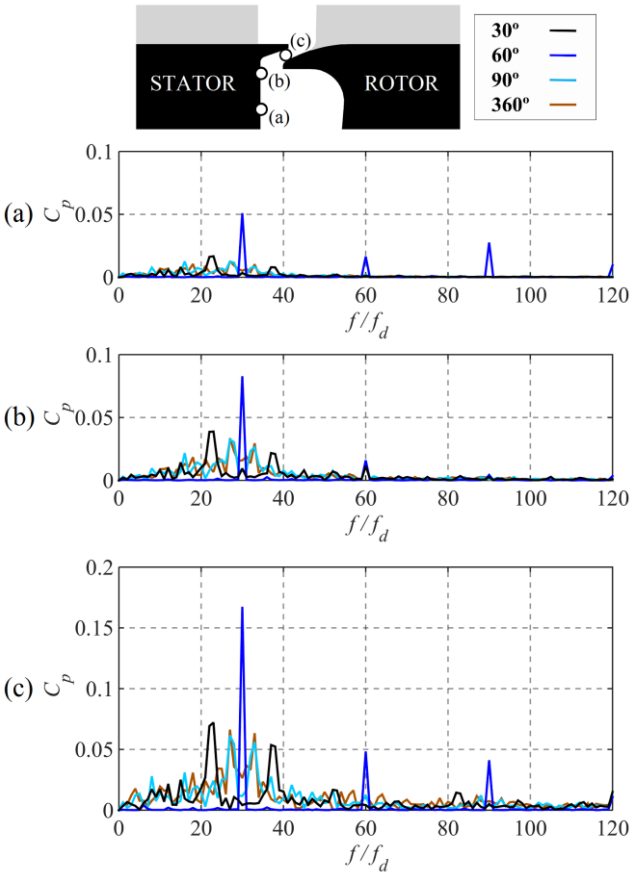

Figure 16: Fast Fourier Transforms of computational data at Φ_0 = 0.050 for four different sector sizes

Overall, similar unsteady structures exist across all the sector sizes used, indicating that computations from these reduced domains can effectively model much of the large-scale unsteadiness associated with rim-seal flows. This is supported by broadly similar time-averaged results across different sectors, as presented in section 4.2 and 4.3. Relative to the full 360º simulation, better accuracy was achieved with the 90º sector over the 30º sector, and a poorer prediction resulted with the 60º sector.

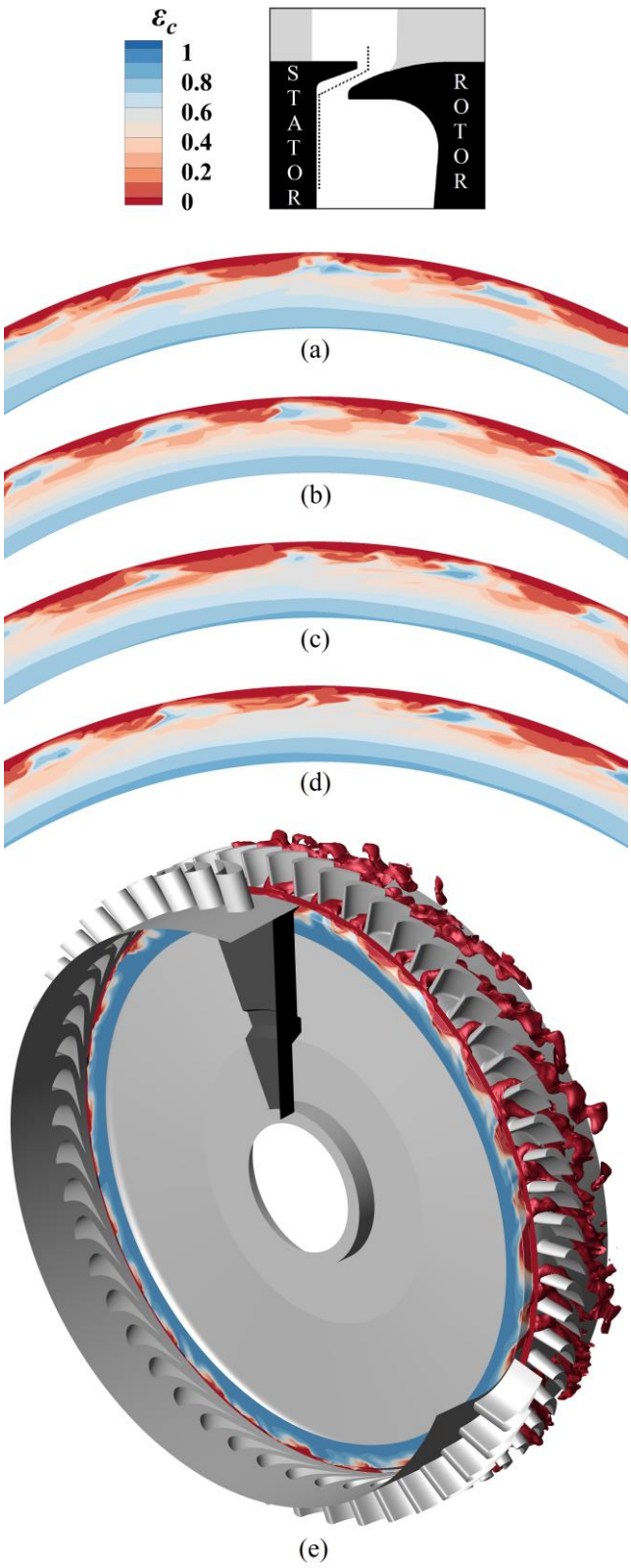

Figure 17: Contours of sealing effectiveness through the chute seal at Φ_0 = 0.050, over a range sector sizes: (a) 30º, (b) 60º, (c) 90º, (d) 360º, (e) 360º with additional iso-surface of ε_c = 0.025

6 CONCLUSIONS

A study of the fluid dynamics of ingress has been undertaken from a scaled axial-turbine incorporating an engine-realistic chute seal, vane and blade geometries. Time-accurate and time-averaged measurements from the 1.5-stage test facility were complemented by Unsteady Reynolds-Averaged Navier-Stokes computations.

- Computations showed good agreement with time-averaged measurements of pressure, swirl and sealing effectiveness.
- An unsteady analysis identified $12 < N < 36$ large-scale structures rotating at a fraction of the disc speed, with good agreement between computation and experiment. The intensity of these instabilities reduced in magnitude at both high and low sealing-flow rates.
- There is supporting evidence that flow instabilities are driven by shear gradients in the seal clearance and that they influence ingress. Shear gradients are strengthened and move radially outward with increasing purge, however, above a threshold egress dominates, blowing instabilities from the seal.
- A gap recirculation within the chute seal interacts directly with the blade leading edge horseshoe vortex, circumferentially displacing features of the secondary flow such as a saddle point.
- A comparison of 30º, 60º, 90º and 360º computational domains show that the steady features of the flow are largely unaffected by the size of the computational sector. Differences in large-scale flow structures were pronounced with the 60º sector and indicate that modelling an even number of blades in small sector simulations should be avoided.

ACKNOWLEDGEMENT

The authors would like to thank Siemens and the Engineering and Physical Sciences Research Council for their financial support. Generous technical support was provided by Kunyuan Zhou and Vincent Peltier of Siemens AG. This research made use of the Balena High Performance Computing Service at the University of Bath.

Data Access: Due to confidentiality agreements with research collaborators, supporting data can only be made available to bona fide researchers subject to a nondisclosure agreement. Details of how to request access are available at the University of Bath data archive.

FUNDING DATA

Engineering and Physical Sciences Research Council (EP/J014826/1).

NOMENCLATURE

A_p	amplitude of unsteady pressure (Pa)
b	radius of seal (m)
BPF	blade passing frequency (Hz)
c	concentration of tracer gas
CFD	computational fluid dynamics
CFL	Courant–Friedrichs–Lewy
C_F	flow coefficient ($=W/(\Omega b)$)
C_p	pressure coefficient ($= A_p / (0.5\,\rho\Omega^2 b^2)$)
$C_{p,a}$	pressure coefficient in annulus ($= (p_a - \bar{p}_a)/(0.5\,\rho\Omega^2 b^2)$)

$C_{p,s}$ pressure coefficient on stator wall

(= $\left(p_a\text{-}p_{ref}\right)/(0.5\,\rho\Omega^2 b^2)$)

$C_{w,0}$ non-dimensional sealing flow rate (= $\dot{m}/(\mu b)$)

DLR Deutsches Zentrum für Luft- und Raumfahrt

f measured frequency (Hz)

f_d frequency of disk rotations (Hz)

FFT fast Fourier transform

G_c seal-clearance ratio (= s_c/b)

GRZ gap recirculation zone

LES large eddy simulation

$\dot{m}$ mass flow rate (kg/s)

M Mach number

N number of large-scale structures around disc

p static pressure (Pa)

r radius (m)

RANS Reynolds-averaged Navier-Stokes

Re_w axial Reynolds number in annulus based on radius (= $\rho W b/\mu$)

Re_ϕ rotational Reynolds number (= $\rho\Omega b^2/\mu$)

RPM revolutions per minute

SST shear stress transport

s_c seal clearance (m)

TET turbine entry temperature

TRACE Turbomachinery Research Aerodynamics Computational Environment

U bulk mean radial seal velocity (= $\dot{m}_0/(2\pi\rho b s_c)$)

URANS unsteady Reynolds-averaged Navier-Stokes simulation

V_ϕ tangential velocity (m/s)

W axial velocity in annulus (m/s)

z axial coordinate (m)

α angle between unsteady pressure transducers (rad)

β swirl ratio (= $V_\phi/(\Omega r)$)

Δt_α time for large scale structure to move through angle α (s)

ε effectiveness

ε_c concentration effectiveness

λ_T turbulent flow parameter (= $C_{w,0}\mathrm{Re}_\phi^{-0.8}$)

μ dynamic viscosity (kg/(ms))

ρ density (kg/m^3)

Φ_0 non-dimensional sealing parameter (= $U/(\Omega b)$)

ω angular speed of large scale structures (rad/s)

Ω angular speed of rotating disk (rad/s)

Subscripts

a annulus

ref reference

s stator wall

0 sealing flow

References

[1] Horwood, J., Hualca, F., Scobie, J., Wilson, M., Sangan, C. and Lock, G., 2018, "Experimental and Computational Investigation of Flow Instabilities in Turbine Rim Seals," ASME J. Eng. Gas Turb. Power, 141(1), pp. 011028-011028-12

[2] Cao, C., Chew, J.W., Millington, P.R. and Hogg, S.I., 2004, "Interaction of rim seal and annulus flows in an axial flow turbine," ASME J. Eng. Gas Turb. Power, 126(4), pp. 786-793.

[3] Beard, P.F., Gao, F., Chana, K.S. and Chew, J., 2017, "Unsteady Flow Phenomena in Turbine Rim Seals," ASME J. Eng. Gas Turb. Power, 139(3), p. 032501.

[4] Patinios, M., Scobie, J.A., Sangan, C.M., Michael Owen, J. and Lock, G.D., 2016, "Measurements and Modeling of Ingress in a New 1.5-Stage Turbine Research Facility," ASME J. Eng. Gas Turb. Power, 139(1), p. 012603.

[5] Dahlqvist, J. and Fridh, J., 2017, "Experimental Investigation of Turbine Stage Flow Field and Performance at Varying Cavity Purge Rates and Operating Speeds," ASME J. Turbomach, 140(3), pp. 031001-031001-10.

[6] Scobie, J. A., Sangan, C. M., Owen, J. M., and Lock, G. D., 2016, "Review of Ingress in Gas Turbines," ASME J. Eng. Gas Turb. Power, 138(12), p. 120801.

[7] Savov, S.S., Atkins, N.R. and Uchida, S., 2017, "A Comparison of Single and Double Lip Rim Seal Geometries," ASME J. Eng. Gas Turb. Power, 139(11), p. 112601.

[8] Mirzamoghadam, A.V., Kanjiyani, S., Riahi, A., Vishnumolakala, R. and Gundeti, L., 2014, "Unsteady 360 Computational Fluid Dynamics Validation of a Turbine Stage Mainstream/Disk Cavity Interaction," ASME J. Turbomach, 137(1), p. 011008.

[9] Scobie, J.A., Teuber, R., Li, Y.S., Sangan, C.M., Wilson, M. and Lock, G.D., 2016, "Design of an Improved Turbine Rim-Seal," ASME J. Eng. Gas Turb. Power, 138(2).

[10] Boudet, J., Hills, N.J. and Chew, J.W., 2006, “Numerical Simulation of the Flow Interaction between Turbine Main Annulus and Disc Cavities,” ASME Paper No. GT2006-90307.

[11] O'Mahoney, T.S.D., Hills, N.J., Chew, J.W. and Scanlon, T., 2011, “Large-Eddy simulation of rim seal ingestion,” Journal of Mechanical Engineering Science, 225(12), pp. 2881-2891.

[12] O'Mahoney, T., Hills, N. and Chew, J., 2012, “Sensitivity of LES results from turbine rim seals to changes in grid resolution and sector size,” Progress in Aerospace Sciences, 52, pp. 48-55.

[13] Julien, S., Lefrancois, J., Dumas, G., Boutet-Blais, G., Lapointe, S., Caron, J.-F. and Marini, R., 2010, “Simulations of flow ingestion and related structures in a turbine disk cavity,” ASME Paper No. GT2010-22729.

[14] Boutet-Blais, G., Lefrancois, J., Dumas, G., Julien, S., Harvey, J.-F., Marini, R. and Caron, J.-F., 2011, “Passive Tracer Validity for Cooling Effectiveness Through Flow Computation in a Turbine Rim Seal Environment,” ASME Paper No. GT2011-45654.

[15] Feiereisen, J., Paolillo, R. and Wagner, J., 2000, “UTRC Turbine Rim Seal Ingestion and Platform Cooling Experiments,” AIAA Paper No. AIAA-2000-3371.

[16] Gao, F., Poujol, N., Chew, J.W. and Beard, P.F., 2018, “Advanced Numerical Simulation of Turbine Rim Seal Flows and Consideration for RANS Turbulence Modelling,” ASME Paper No. GT2018-75116

[17] Ko, S.H. and Rhode, D.L., 1992, “Thermal Details in a Rotor–Stator Cavity at Engine Conditions With a Mainstream,” ASME J. Turbomach., 114(2), pp. 446-453.

[18] Savov, S.S. and Atkins, N.R., 2017, "A Rim Seal Ingress Model Based on Turbulent Transport," ASME Paper No. GT2017- 63531.

[19] Chilla, M., Hodson, H. and Newman, D., 2013, "Unsteady interaction between annulus and turbine rim seal flows," ASME J. Turbomach., 135(5), p. 051024.

[20] Green, B.R., Mathison, R.M. and Dunn, M.G., 2014, "Time-averaged and time-accurate aerodynamic effects of forward rotor cavity purge flow for a high-pressure turbine-part I: Analytical and experimental comparisons," ASME J. Turbomach., 136(1), p. 011004.

[21] Green, B.R., Mathison, R.M. and Dunn, M.G., 2014, "Time-averaged and time-accurate aerodynamic effects of rotor purge flow for a modern, one and one-half stage high-pressure turbine-Part II: Analytical flow field analysis," ASME J. Turbomach., 136(1), 011009.

[22] Clark, K., Barringer, M., Johnson, D., Thole, K., Grover, E. and Robak, C., 2017, "Effects of Purge Flow Configuration on Sealing Effectiveness in a Rotor-Stator Cavity," ASME Paper No. GT2017-63910.

[23] Berdanier, R.A., Monge-Concepción, I., Knisely, B.F., Barringer, M.D., and Thole, K.A., 2018, "Scaling Sealing Effectiveness in a Stator-Rotor Cavity for Differing Blade Spans," ASME Paper No. GT2018-77105.

[24] Roy, R.P., Feng, J., Narzary, D. and Paolillo, R.E., 2005, "Experiment on Gas Ingestion Through Axial-Flow Turbine Rim Seals," ASME J. Eng. Gas Turb. Power, 127(3), pp. 573-582.

[25] Teuber, R., Li, Y.S., Maltson, J., Wilson, M., Lock, G.D. and Owen, J.M., 2013, "Computational extrapolation of turbine sealing effectiveness from test rig to engine conditions," Proceedings of the Institution of Mechanical Engineers, Part A: Journal of Power and Energy, 227(2), pp. 167-178.

[26] Schadler, R., Kalfas, A.I., Abhari, R.S., Schmid, G. and Voelker, S., 2017, "Modulation and radial migration of turbine hub cavity modes by the rim seal purge flow," ASME J. Turbomach., 139(1), p. 011011.

[27] Jakoby, R., Zierer, T., Lindblad, K., Larsson, J., deVito, L., Bohn, D. E., Funcke, J., and Decker, A., 2004, "Numerical Simulation of the Unsteady Flow Field in an Axial Gas Turbine Rim Seal Configuration," ASME Paper No. GT2004-53829.

[28] Pogorelov, A., Meinke, M. and Schröder, W., 2018, "Large-Eddy Simulation of the Unsteady Full 3D Rim Seal Flow in a One-Stage Axial-Flow Turbine," Flow, Turbulence and Combustion. DOI: 10.1007/s10494-018-9956-9

[29] Wang, C.-Z., Mathiyalagan, S., Johnson, B.V., Glahn, J.A. and Cloud, D.F., 2014, "Rim seal ingestion in a turbine stage from 360 degree time-dependent numerical simulations". ASME J. Turbomach., 136(3), p. 031007.

[30] Zhou, D.W., Roy, R.P., Wang, C.Z. and Glahn, J.A., 2010, "Main Gas Ingestion in a Turbine Stage for Three Rim Cavity Configurations," ASME J. Turbomach., 133(3), pp. 031023-031023-12.

[31] Owen, J. M., and Rogers, R. H., 1989, Flow and Heat Transfer in Rotating-Disc Systems, Volume 1—Rotor Stator Systems, Research Studies Press Ltd, Taunton, UK.

[32] Da Soghe, R., Bianchini, C., Sangan, C.M., Scobie, J.A. and Lock, G.D., 2016, "Numerical Characterization of Hot-Gas Ingestion Through Turbine Rim Seals," ASME J. Eng. Gas Turb. Power, 139(3), pp. 032602-032602-9

[33] Rabs, M., Benra, F.K., Dohmen, H.J. and Schneider, O., 2009, "Investigation of flow instabilities near the rim cavity of a 1.5 stage gas turbine," ASME Paper No. GT2009-59965.

[34] Gentilhomme, O., Hills, N.J., Turner, A.B. and Chew, J.W., 2003, "Measurement and Analysis of Ingestion Through a Turbine Rim Seal," ASME J. Turbomach., 125(3), pp. 505-512.

[35] Boudet, J., Autef, V., Chew, J., Hills, N. and Gentilhomme, O., 2005, "Numerical simulation of rim seal flows in axial turbines," Aeronautical Journal, 109(1098), pp. 373-383.

[36] Hualca, F., Horwood, J., Scobie, J., Sangan, C. and Lock, G., 2019, "The Effect of Vanes and Blades on Ingress in Gas Turbines," ASME Paper No. GT2019-90987.

[37] Gao, F., Chew, J., Beard, P.F., Amirante, D. and Hills, N.J., 2017, "Numerical Studies of Turbine Rim Sealing Flows on a Chute Seal Configuration," Proceedings of 12th European Conference on Turbomachinery Fluid dynamics & Thermodynamics, p. ETC2017-284.

[38] Town, J., Averbach, M. and Camci, C., 2016, "Experimental and Numerical Investigation of Unsteady Structures Within the Rim Seal Cavity in the Presence of Purge Mass Flow," ASME Paper No. GT2016-56500.